The Astrophysical Journal, 769:144 (13pp), 2013 June 1 doi:10.1088/0004-637X/769/2/144


# EXTRAPOLATION OF THE SOLAR CORONAL MAGNETIC FIELD FROM *SDO*/HMI MAGNETOGRAM BY A CESE–MHD–NLFFF CODE

Chaowei Jiang (江朝伟) and Xueshang Feng (冯学尚)
SIGMA Weather Group, State Key Laboratory for Space Weather, Center for Space Science and Applied Research, Chinese Academy of Sciences, Beijing 100190, China; cwjiang@spaceweather.ac.cn, fengx@spaceweather.ac.cn
*Received 2013 January 5; accepted 2013 April 8; published 2013 May 15*

## ABSTRACT

Due to the absence of direct measurement, the magnetic field in the solar corona is usually extrapolated from the photosphere in a numerical way. At the moment, the nonlinear force-free field (NLFFF) model dominates the physical models for field extrapolation in the low corona. Recently, we have developed a new NLFFF model with MHD relaxation to reconstruct the coronal magnetic field. This method is based on CESE–MHD model with the conservation-element/solution-element (CESE) spacetime scheme. In this paper, we report the application of the CESE–MHD–NLFFF code to *Solar Dynamics Observatory*/Helioseismic and Magnetic Imager (*SDO*/HMI) data with magnetograms sampled for two active regions (ARs), NOAA AR 11158 and 11283, both of which were very non-potential, producing X-class flares and eruptions. The raw magnetograms are preprocessed to remove the force and then inputted into the extrapolation code. Qualitative comparison of the results with the *SDO*/AIA images shows that our code can reconstruct magnetic field lines resembling the EUV-observed coronal loops. Most important structures of the ARs are reproduced excellently, like the highly sheared field lines that suspend filaments in AR 11158 and twisted flux rope which corresponds to a sigmoid in AR 11283. Quantitative assessment of the results shows that the force-free constraint is fulfilled very well in the strong-field regions but apparently not that well in the weak-field regions because of data noise and numerical errors in the small currents.

*Key words:* magnetic fields – magnetohydrodynamics (MHD) – methods: numerical – Sun: corona

*Online-only material:* color figures

## 1. INTRODUCTION

Magnetic field extrapolation is an important tool to study the three-dimensional (3D) solar coronal magnetic field, which is still difficult to measure directly (Sakurai 1989; Aly 1989; Amari et al. 1997; McClymont et al. 1997; Wiegelmann 2008; DeRosa et al. 2009). The most popular models being used for field extrapolation are the potential field model, the linear force-free field model, and the nonlinear force-free field (NLFFF) model. These models are all based on the same assumption that the Lorentz force is self-balancing in the corona, but adopt different simplifications of the current distribution. Among these models, the NLFFF is the most used for characterizing magnetic field in the low corona, where there is significant and localized electric current, especially in the active regions (ARs).

But, directly solving the general NLFFF equation

$$(\nabla \times \mathbf{B}) \times \mathbf{B} = \mathbf{0}, \quad \nabla \cdot \mathbf{B} = 0 \tag{1}$$

is very difficult. As is known, the system is nonlinear intrinsically and even the existence and uniqueness of a solution for a given boundary condition are not proven theoretically; solutions have rarely been found in closed analytic form (e.g., Low & Lou 1990) and in most cases the numerical method requires the use of a computer (many numerical codes have been developed in the past few decades, e.g., Wu et al. 1990; Roumeliotis 1996; Amari et al. 1999; Wheatland et al. 2000; Yan & Sakurai 2000; Wiegelmann 2004; Valori et al. 2007; Inoue et al. 2011; one may refer to a recent review by Wiegelmann & Sakurai 2012). Moreover, observation can only provide a bottom boundary of data, and, even worse, on the photosphere the field is forced significantly by the dense plasma and thus conflicts with the fundamental force-free assumption. Besides the noise in observations, measurement error and instrumental uncertainty (e.g., the well known 180° ambiguity of the transverse fields) are all rather unfavorable for practical computation. Thus the observed magnetogram usually needs to be preprocessed to remove the force and noise for providing a better input (Wiegelmann et al. 2006). As a result, at present it is difficult to seek an exact force-free solution with the observation information fully satisfied. The best case scenario is to find a good balance between the force-free constraint and deviation from the real observation, i.e., to seek an approximately force-free solution that matches the photospheric field measurements as well as possible.

Recently we have developed a new extrapolation code called CESE–MHD–NLFFF[1] (Jiang et al. 2011; Jiang & Feng 2012), which is based on a magnetohydrodynamics (MHD) relaxation method and an advanced numerical scheme, the spacetime conservation-element/solution-element (CESE) method, for faster convergence and better accuracy over the available codes. The good performance and high accuracy of the code have been demonstrated through critical comparisons with previous joint studies by Schrijver et al. (2006) and Metcalf et al. (2008), in which various NLFFF codes are assessed based on several NLFFF benchmark tests. We have also successfully extended the code to application in spherical geometry and seamless full-sphere extrapolation for the global corona (Jiang et al. 2012b).

In this paper we report the application of the CESE–MHD–NLFFF code to real solar data, i.e., the presently released

[1] We initially planned to develop a full MHD model for computing both the static non-potential field and dynamic evolution of ARs (i.e., the CESE–MHD model; Jiang et al. 2011). However, we find that the MHD solver is rather slow to construct the static field, although success has been reported in Jiang et al. (2012a). We thus move to develop an NLFFF version of this model for a faster convergence speed, while the full MHD solver is more suitable for simulating transient events like the eruptions.

*Solar Dynamics Observatory*/Helioseismic and Magnetic Imager (*SDO*/HMI) magnetograms. To deal with the real observation data, we also have developed a new preprocessing method to remove the force in the raw magnetogram (C. W. Jiang & X. S. Feng 2013, in preparation). Additional advancements are made to the original code to further enhance the ability of handling the high-resolution but noisy data. Magnetograms of two ARs, AR 11158 and AR 11283 are sampled for our tests of extrapolation. The results are carefully assessed both qualitatively and quantitatively. We show that our code can recover magnetic field lines resembling the plasma loops seen in the *SDO*/AIA images, and reproduce most important structures of the ARs remarkably well such as the highly sheared field lines that suspend filaments in AR 11158 and the twisted flux rope that corresponds to a sigmoid in AR 11283.

The remainder of the paper is organized as follows. We first briefly describe the CESE–MHD–NLFFF code along with its improvements in Section 2. The magnetogram from *SDO*/HMI and the preprocessed result of the raw data are given in Section 3. We then present the extrapolation results for these data including both the raw and preprocessed magnetogram in Section 4. Finally, we draw conclusions and present some outlooks for future work in Section 5.

## 2. THE CESE–MHD–NLFFF CODE

The basic idea of using the MHD relaxation approach to solve the force-free field is to use some kind of fictitious dissipation to drive the MHD system to an equilibrium in which all the forces can be neglected comparing with the Lorentz force while the boundary magnetogram is satisfied. In this way the Lorentz force should be self-balancing and the field can be regarded as the target force-free solution. We solve the magnetofrictional model equations in the magnetic splitting form as

$$\begin{aligned}\frac{\partial \rho \mathbf{v}}{\partial t} &= (\nabla \times \mathbf{B}_1) \times \mathbf{B} - (\nabla \cdot \mathbf{B}_1)\mathbf{B} - \nu \rho \mathbf{v},\\ \frac{\partial \mathbf{B_1}}{\partial t} &= \nabla \times (\mathbf{v} \times \mathbf{B}) + \nabla(\mu \nabla \cdot \mathbf{B}_1) - \mathbf{v}\nabla \cdot \mathbf{B}_1,\\ \rho &= |\mathbf{B}|^2 + \rho_0,\ \mathbf{B} = \mathbf{B}_0 + \mathbf{B}_1. \end{aligned} \quad (2)$$

Here, $\mathbf{B}$ is the target force-free field to be solved, $\mathbf{B}_0$ is the potential field matching the normal component of the magnetogram, and $\mathbf{B}_1$ is the deviation between $\mathbf{B}$ and $\mathbf{B}_0$. $\nu$ is the frictional coefficient and $\mu$ is the numerical diffusive speed of the magnetic monopole. Their values are, respectively, given by $\nu = 1/(5\Delta t)$ and $\mu = 0.4(\Delta x)^2/\Delta t$ in the code, according to the time step $\Delta t$ and local grid size $\Delta x$. Many advantages can be gained by solving such form of the above equations (Jiang & Feng 2012; Jiang et al. 2012b).

The above equation system (2) is solved by our CESE–MHD scheme (Jiang et al. 2010). In principle we can use any available MHD code to solve this set of equations since it is a subset of the full MHD system. Taking into consideration computational efficiency and accuracy, we prefer to utilize modern advanced MHD codes. However, most modern MHD codes are based on a theory of characteristic decomposition of a hyperbolic system, and thus are not suitable for Equation (2), which is not a hyperbolic system. The CESE scheme is a new method free of characteristic decomposition and is very suitable for the equation form here. Furthermore, the CESE-MHD code has been extensively used in solar physics, e.g., the data-driven evolution modeling of AR (Jiang et al. 2012a), the global corona (Feng et al. 2012), and the interplanetary solar wind (Feng et al. 2012; Yang et al. 2012).

To adapt for the application to real solar data, we made additional improvements to the previous version of CESE–MHD–NLFFF. The first improvement is made to enhance the ability of handling noisy data in the magnetograms. In the noisy weak-field regions of magnetograms (where the signal-to-noise ratio is small, about $|\mathbf{B}| \leqslant 100$ G), the term $(\nabla \times \mathbf{B}) \times \mathbf{B}/|\mathbf{B}|^2$ could be very large due to numerical gradients of the random noise, thus the velocity $\mathbf{v}$ is prone to being accelerated extremely high, which can severely restrict the time step and slow the relaxation process of the entire system, even making computation unmanageable. To deal with this difficulty, the pseudo-plasma density $\rho$ is designed with $\rho_0 = B_{\rm min}^2 \exp(-z/H_{\rm m})$, where $z$ is the height from the bottom surface and $B_{\rm min} = 100$ G, $H_{\rm m} = 5$ pixel. In this way, the velocity (near the bottom magnetogram) in the weak-field regions can be reduced significantly, while it is barely affected in the strong-field regions.

Second, to deal with high-resolution observation data, the extrapolation is performed on a non-uniform grid within a block-structured, distributed-memory parallel computational framework (e.g., Jiang et al. 2012a). Specifically, the whole computational volume is divided into blocks with different spatial resolution, and the blocks are evenly distributed among the processors. Within this framework, we have a great amount of freedom to configure the mesh and save computational resources comparing with a uniform grid. As concentrated strongly in the photosphere but expanding rapidly into the corona due to an abrupt drop in gas pressure, the coronal field becomes smoother and weaker successively with height. Naturally, we use a grid with decreasing resolution with height: at the bottom the grid the spacing matches the resolution of the magnetogram and at the top of the model box the grid spacing is increased by about four times. At present we use the same resolution in the horizontal plane, and application of adaptive resolution based on the pattern of magnetic flux distribution is under development. With this framework, we also add some coarse buffer blocks around the central volume to reduce influence by the numerical boundaries without adding much computational burden. An example of the grid is shown in Figure 1.

The quantities in the computational volume are routinely initialized by setting $\mathbf{B}_1 = \mathbf{0}$ and $\mathbf{v} = \mathbf{0}$. The potential field $\mathbf{B}_0$ is obtained by a Green's function method (e.g., Metcalf et al. 2008). The bottom boundary is incrementally fed with the observed vector magnetogram in tens of Alfvén time $\tau_{\rm A}$, while all the other numerical boundaries are fixed with $\mathbf{B}_1 = \mathbf{0}$ and $\mathbf{v} = \mathbf{0}$.

## 3. DATA

### 3.1. The HMI Data

The HMI on board the *SDO* provides photospheric vector magnetograms with a high resolution both in space and time. It observes the full Sun with a 4 K × 4 K CCD whose spatial sampling is 0.5 arcsec pixel$^{-1}$. Raw filtergrams are obtained at six different wavelengths and six polarization states in the Fe I 6173 Å absorption line, and are collected and converted into observable quantities (such as Dopplergrams, continuum filtergrams, and line-of-sight and vector magnetograms) on a rapid time cadence. For the vector magnetic data, each set of filtergrams takes 135 s to be completed. To obtain vector magnetograms, Stokes parameters are first derived from

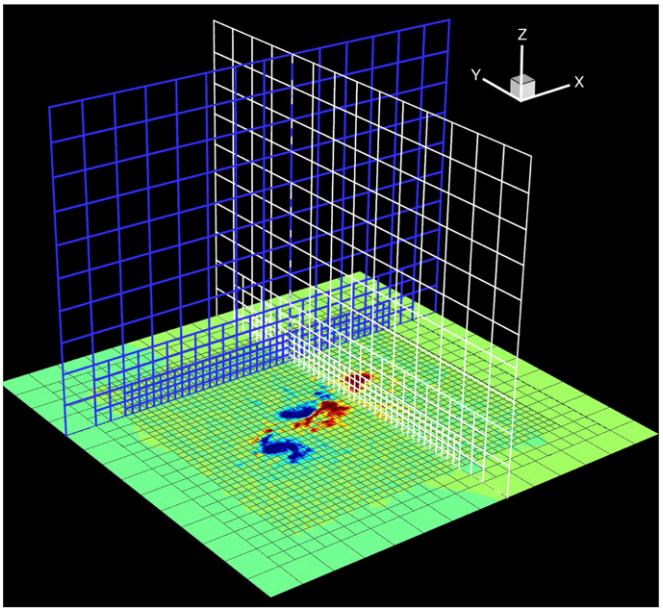


**Figure 1.** Grid structure: the entire volume is divided into blocks and each block has $8 \times 8 \times 8$ cells. Slices through the volume in three axis directions are plotted to show the structure of the blocks and the bottom contour map represents $B_z$ on the photosphere.

(A color version of this figure is available in the online journal.)

**Table 1**
Quality of the Magnetograms

| Data | $\epsilon_{\rm flux}$ | $\epsilon_{\rm force}$ | $\epsilon_{\rm torque}$ | $S_x$ | $S_y$ | $S_z$ |
|---|---|---|---|---|---|---|
| AR 11158 | | | | | | |
| Raw map | 0.017 | 0.072 | 0.073 | 5.05E-03 | 6.12E-03 | 1.05E-03 |
| Preprocessed map | 0.019 | 0.002 | 0.002 | 7.83E-05 | 1.01E-04 | 8.74E-05 |
| Numerical potential | 0.019 | 0.001 | 0.002 | 8.78E-05 | 8.42E-05 | 8.74E-05 |
| AR 11283 | | | | | | |
| Raw map | −0.111 | 0.193 | 0.143 | 1.12E-02 | 1.15E-02 | 1.94E-03 |
| Preprocessed map | −0.119 | 0.012 | 0.017 | 1.73E-04 | 1.95E-04 | 1.79E-04 |
| Numerical potential | −0.119 | 0.011 | 0.017 | 1.98E-04 | 1.63E-04 | 1.79E-04 |

filtergrams observed over a 12 minute interval and then inverted through the Very Fast Inversion of the Stokes Vector (Borrero et al. 2011). The 180° azimuthal ambiguity in the transverse field is resolved by an improved version of the "minimum energy" algorithm (Leka et al. 2009). Regions of interest with strong magnetic fields are automatically identified near real time (Turmon et al. 2010). A detailed description on how the vector magnetograms are produced can be found on the Web site http://jsoc.stanford.edu/jsocwiki/VectorPaper.

The magnetogram data we use here is downloaded from http://jsoc.stanford.edu/jsocwiki/VectorPaper, where the HMI vector magnetic field data series `hmi.B_720s_e15w1332` are released for several ARs. There are two special formats, i.e., direct cutouts and remapped images. We use the remapped format which is more suitable for modeling in local Cartesian coordinates, since the images are computed with a Lambert cylindrical equal area projection centered on the tracked region. For our test, we select two ARs, AR 11158 and AR 11283, both of which produced X-class flares and were very non-potential. The full resolution of the data is about $0\farcs5$ pixel$^{-1}$ and we rebin them to $1''$ pixel$^{-1}$ for the NLFFF modeling.

AR 11158 is a well-known target studied in many recent works for different purposes (e.g., Schrijver et al. 2011; Sun et al. 2012b; Liu et al. 2012; Jing et al. 2012), and was selected

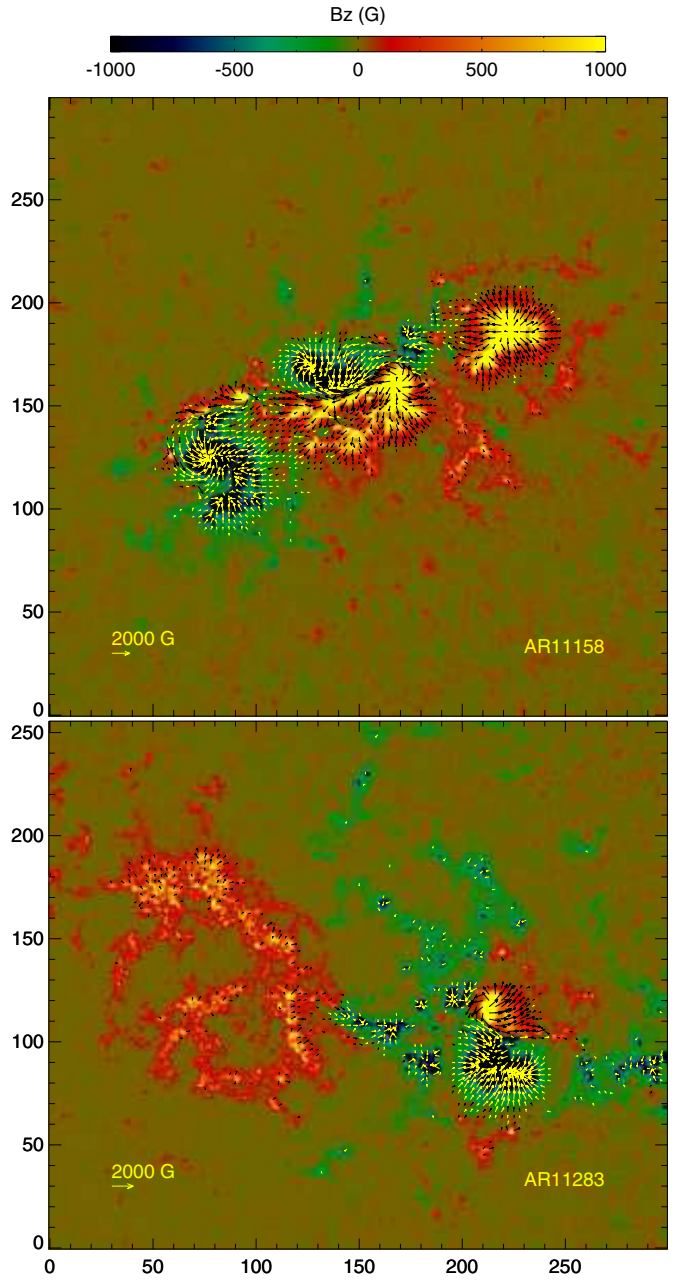


**Figure 2.** Vector magnetograms for AR 11158 and AR 11283. The background shows the vertical components with saturation values of ±1000 G; the vectors represent the transverse fields (above 200 G). The length unit is arcsec.

(A color version of this figure is available in the online journal.)

by Wiegelmann et al. (2012) for a special test on optimizing their extrapolation code with HMI data. This AR has a multipolar and complex structure. It produced several major flares and coronal mass ejections (CMEs) during its disk passage, including the first X-class flare of cycle 24 on 2012 February 15. Figure 2 (the top panel) shows a vector magnetogram of AR 11158 taken at 20:36 UT on 2011 February 14, which will be used for our computation. This AR is well isolated from others and is almost flux-balanced (see Table 1), with the main polarities concentrated in the central field of view (FoV). As can be seen, the field shows a strong shearing along the polarity inversion lines (PILs).

The other AR, AR 11283, is also very eruptive, generating several X-class flares and CMEs. We select a magnetogram

taken at 22:00 UT on September 6, just prior to a major flare at 22:20 UT. The magnetogram is shown in the bottom panel of Figure 2. As an input for extrapolation, this data is not as good as AR 11158's, since the flux is dispersed with some strong polarities almost on the edge of the FoV. In addition, the total flux is not well balanced (see Table 1), which is unfavorable for our extrapolation.

### 3.2. Data Preprocessing

Generally, the raw magnetogram cannot be inputted directly into the NLFFF code because the photospheric field is intrinsically non-force-free and violates the force-free assumption. According to the derivation by Molodenskii (1969) and Aly (1989), an ideally force-free magnetogram should fulfill the following conditions:

$$\int_S B_z\,dx\,dy = 0, \quad F_x = \int_S B_x B_z\,dx\,dy = 0,$$
$$F_y = \int_S B_y B_z\,dx\,dy = 0, \quad F_z = \int_S E_B\,dx\,dy = 0,$$
$$T_x = \int_S y E_B\,dx\,dy = 0, \quad T_y = \int_S x E_B\,dx\,dy = 0,$$
$$T_z = \int_S (y B_x B_z - x B_y B_z)\,dx\,dy = 0 \quad (3)$$

where $E_B = B_x^2 + B_y^2 - B_z^2$. These expressions are derived from the volume integrals of the total divergence, magnetic force, and torque of an ideally force-free field

$$\int_V \nabla\cdot\mathbf{B}\,dV = 0, \quad \int_V \mathbf{j}\times\mathbf{B}\,dV = \mathbf{0}, \quad \int_V \mathbf{r}\times(\mathbf{j}\times\mathbf{B})\,dV = \mathbf{0} \quad (4)$$

(by using Gauss' divergence theorem, the volume integrals 4 can be transformed to the surface integrals 3). In the case of the coronal field, the surface integrals of Equation (3) are usually restricted within the bottom magnetogram since the contribution from other boundaries can be neglected. To assess the real data with respect to the force-free condition, three parameters are usually computed as (Wiegelmann et al. 2006)

$$\epsilon_{\rm flux} = \frac{\int_S B_z\,dx\,dy}{\int_S |B_z|\,dx\,dy}, \quad \epsilon_{\rm force} = \frac{|F_x| + |F_y| + |F_z|}{\int_S P_B\,dx\,dy},$$
$$\epsilon_{\rm torque} = \frac{|T_x + |T_y| + |T_z|}{\int_S \sqrt{x^2+y^2}P_B\,dx\,dy}, \quad (5)$$

where $P_B = B_x^2 + B_y^2 + B_z^2$. Small values of these quantities, e.g., $\epsilon_{\rm flux}, \epsilon_{\rm force}, \epsilon_{\rm torque} \ll 1$ indicate a good input for the NLFFF modeling. Table 1 shows that for AR 11158, the force-free condition is satisfied quite well with flux almost balanced and $\epsilon_{\rm force}, \epsilon_{\rm torque}$ less than 0.1; however, for AR 11283, it is worse. Note that the flux non-balance will have a negative effect on the extrapolation (see Section 4).

Besides being non-force-free, the observed data contains measurement noise which is also unfavorable for practical implementation of extrapolation. To this end, preprocessing of the raw magnetogram has been proposed by Wiegelmann et al. (2006) to remove the force and noise for providing better input for NLFFF modeling. To be consistent with our extrapolation code using a magnetic splitting form, we recently developed a new code for magnetogram preprocessing (C. W. Jiang & X. S. Feng 2013, in preparation), in which the vector magnetogram is also split into two parts for a potential field and a non-potential field; we deal with the two parts separately. Preprocessing of the potential part is simply performed by taking the data sliced at a plane about 400 km above the photosphere[2] from the 3D potential field which is extrapolated from the observed vertical field. Then the non-potential part is modified and smoothed by an optimization method to fulfill the constraints of total magnetic force-freeness and torque-freeness, which is similar to the method proposed by Wiegelmann et al. (2006). We have paid particular attention to what extent the force needs to be removed and the data can be smoothed. As for practical computation based on numerical discretization, an accurate satisfaction of force-free constraints is apparently not necessary. Also the extent of the smoothing for the data must be carefully determined in order to mimic the expansion of the magnetic field from the photosphere to some specific height. We use the force-free and smooth values calculated from the preprocessed potential-field part as a reference to guide the preprocessing of the non-potential field part, i.e., we require that the target magnetogram has the same force-free and smoothness levels as its potential part. These requirements can well restrict the free parameters, i.e., the weighted factors in the optimization function.

The results of preprocessed data are also given in Table 1 together with results of its numerical potential-field part. For both magnetograms, the preprocessing reduces the parameters $\epsilon_{\rm force}$ and $\epsilon_{\rm torque}$ by more than one order of magnitude, making the residual force around the level of numerical error (i.e., the parameters are close to those of the numerical potential field). The parameters $S_x, S_y, S_z$ in the table measure the smoothness of the components $B_m$ ($m = x, y, z$), which are defined by (see C. W. Jiang & X. S. Feng 2013, in preparation)

$$S_m = \sum_{\rm p}[(\Delta B_m)^2] \Big/ \sum_{\rm p}[(\bar{\Delta} B_m)^2] \quad (6)$$

where the summation $\sum_{\rm p}$ is over all the pixels of the magnetogram, and $\Delta$ is a typical five-point two-dimensional-Laplace operator, i.e., for pixel $(i, j)$

$$\Delta B_{i,j} \equiv B_{i+1,j} + B_{i-1,j} + B_{i,j+1} + B_{i,j-1} - 4B_{i,j},$$
$$\bar{\Delta} B_{i,j} \equiv B_{i+1,j} + B_{i-1,j} + B_{i,j+1} + B_{i,j-1} + 4B_{i,j}. \quad (7)$$

As shown, the smoothness of the preprocessed data is very close to those of their potential parts, and is consistent among three components, which is unlike the raw data with very different smoothness for different components. Smoothing of the data can be clearly seen by comparing the raw and preprocessed magnetograms as shown in Figures 3 and 4, and especially in the $J_z$ map which shows that the random noise is suppressed effectively (but not entirely).

Note that the constraints of Equation (3) are only necessary conditions, but not sufficient for an ideally force-free magnetogram, meaning that the magnetogram may still contain force even when these conditions are satisfied. However, we can say that the preprocessed magnetogram is more suitable for NLFFF modeling than the raw data, but it is not a completely consistent boundary condition.

[2] We choose this height because the field becomes force-free in the chromosphere roughly 400 km above the photosphere according to Metcalf et al. (1995). Our preprocessing code is designed to modify the photospheric magnetogram to mimic a force-free chromospheric magnetogram at this height.

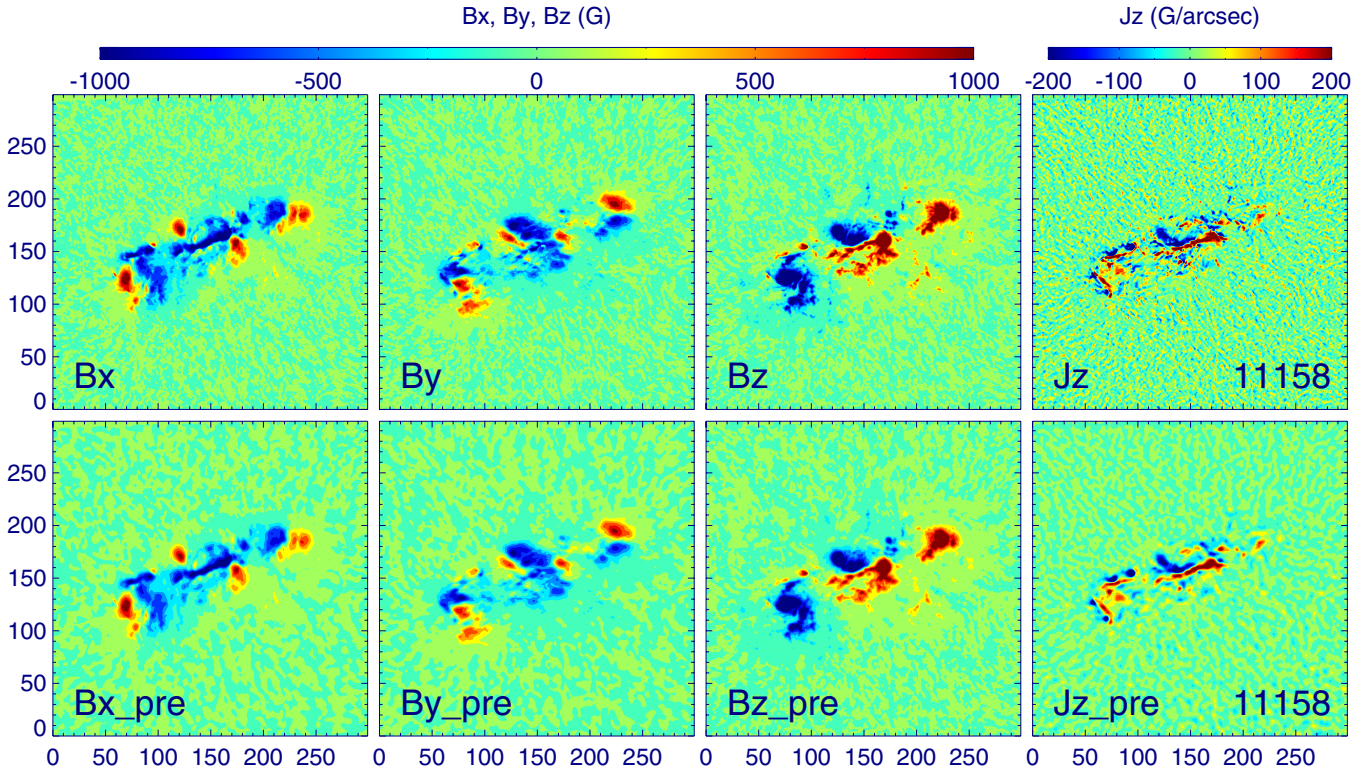


**Figure 3.** Raw and preprocessed magnetograms for AR 11158.
(A color version of this figure is available in the online journal.)

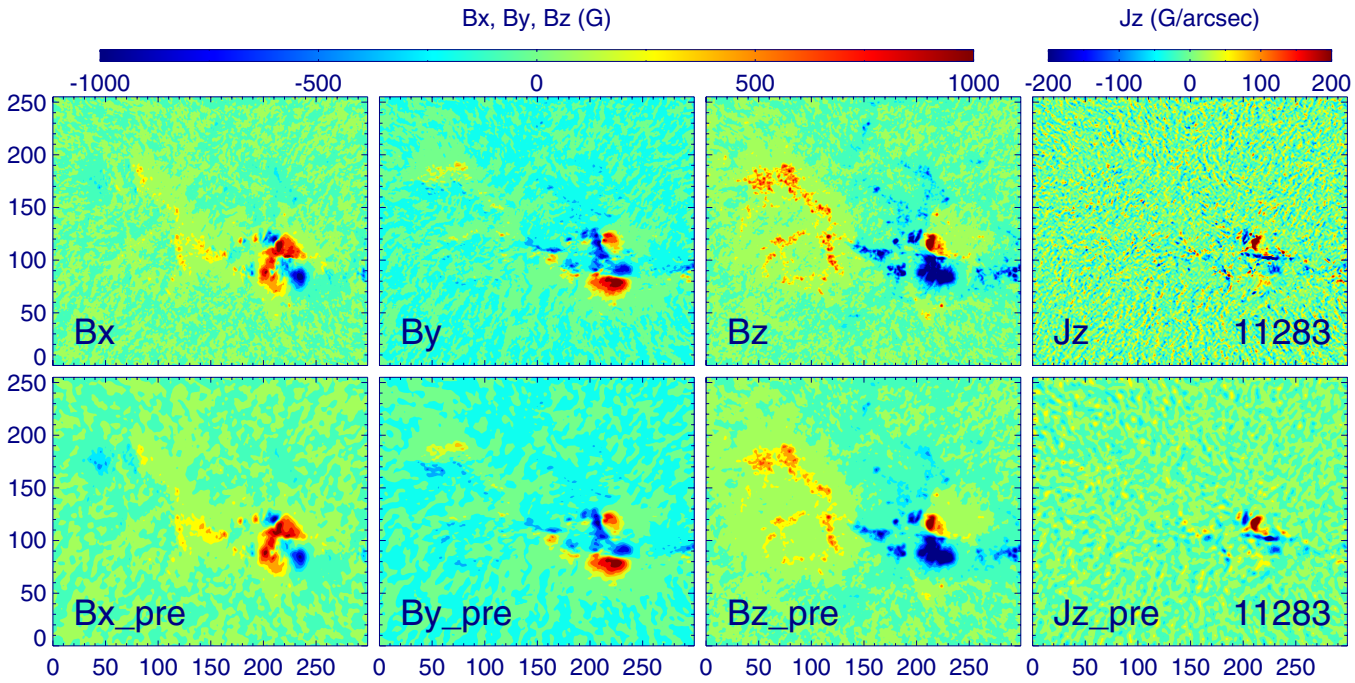


**Figure 4.** Raw and preprocessed magnetograms for AR 11283.
(A color version of this figure is available in the online journal.)

## 4. RESULTS

### *4.1. AR 11158*

The observed coronal loops in X-ray and EUV images give us a proxy of the magnetic field line geometry and are thus a good constraint for the magnetic field model besides the vector magnetograms (e.g., Aschwanden et al. 2012; Malanushenko et al. 2012). In Figure 5 we compare the extrapolated field with coronal loops observed by *SDO*/AIA in the wavelength of 171 Å, in which the loops are the most visible compared to other channels. The field lines are traced from the photosphere at locations selected roughly according to the footpoints of the

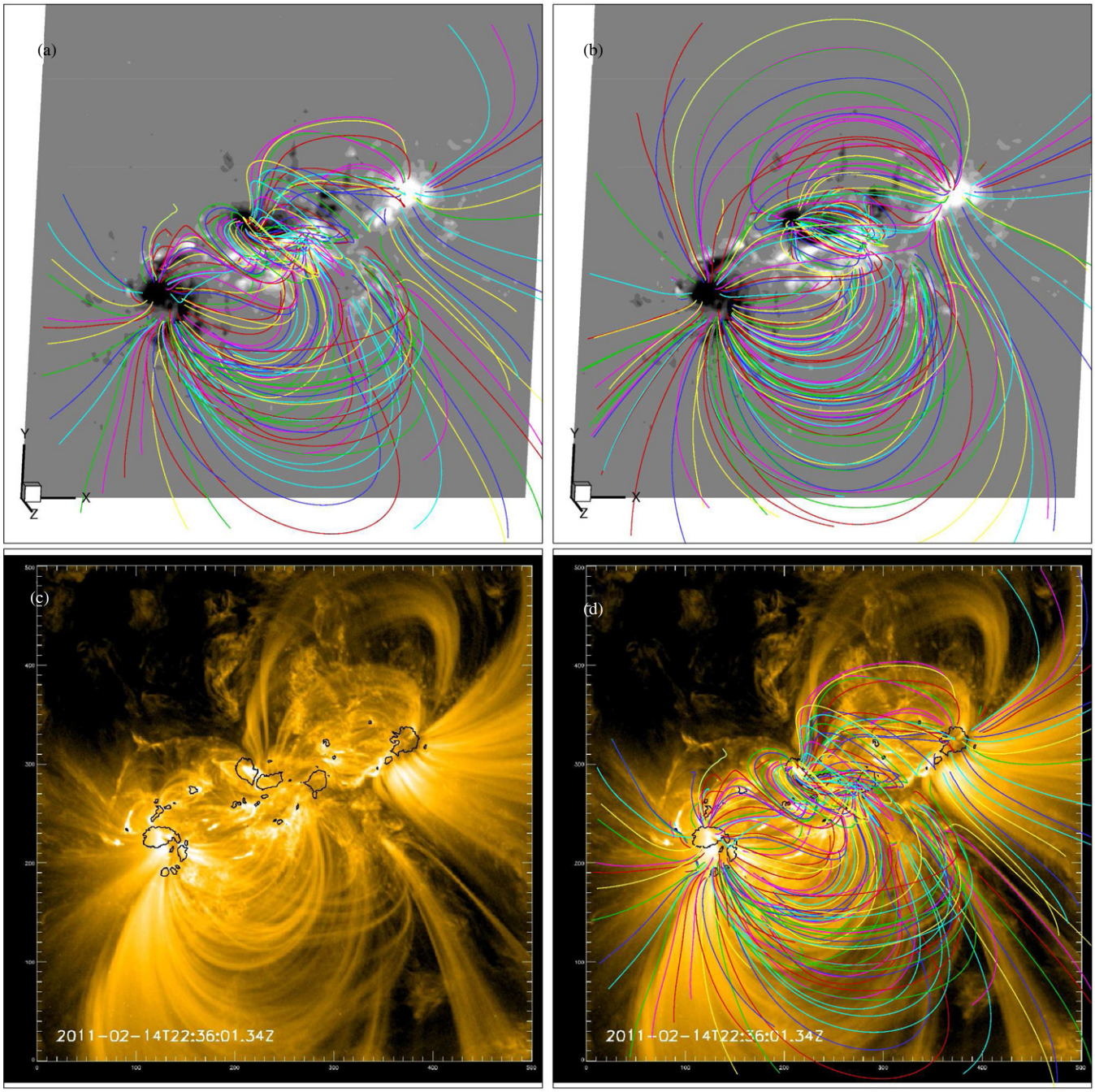


**Figure 5.** Comparison of extrapolation field lines with AIA 171 Å loops for AR 11158: the NLFFF lines (a), the potential field lines (b), the AIA image (c) and NLFFF lines overlaying the AIA image (d). Contour lines for ±1000 G (the black curves) of line-of-sight photospheric field are overplotted on the AIA images, and for all the panels the field lines are traced from the same set of footpoints on the bottom surface.

(A color version of this figure is available in the online journal.)

visible bright loops, and are rendered with different colors for clarity. The viewing angle of the field lines is aligned with the AIA image. We plot the field lines and the AIA image both alone and overlaid for better inspection of the result. As shown from an overview of the images, most of the extrapolated field lines closely resemble the observed loops. At the central region the field lines are strongly sheared along the major PIL and slightly twisted (as compared with the potential solution), indicating the existence of strong electric currents along the field lines. In the left panel of Figure 6, we plot an image of vertical integral of the current density in the extrapolation volume, and the strong-current regions are outlined by the boxes (labeled as A, B, and C). Note that the currents are strongly localized within the central region B and a smaller region C. The magnetic structures of the strong-current regions are shown in the right panel of Figure 6. As can be seen, the twist of the field lines in region C is much stronger than that in region B. The results support observational studies that show that a filament related to an X-class flare and CME exists in the core region B (Sun et al. 2012b), and there are small eruptions in region C due to flux emergence (Sun et al. 2012a).

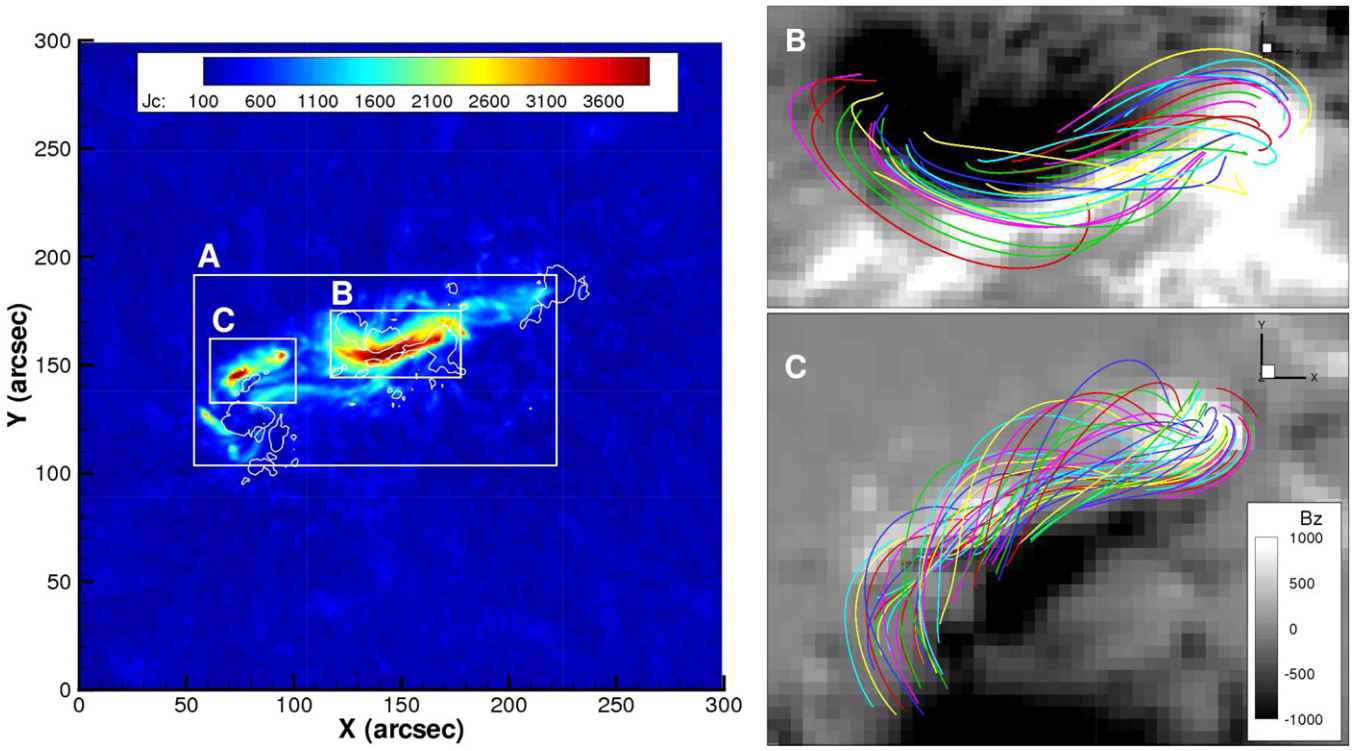


**Figure 6.** Strong-current regions and their magnetic structures for AR 11158. The left panel is an image of the vertical integral of current density, i.e., $J_C = \int |\mathbf{J}| dz$ where the current is calculated by $\mathbf{J} = \nabla \times \mathbf{B}$ with a unit of G pixel$^{-1}$; Regions of strong current are outlined by the boxes A, B, and C. The right panels show the magnetic structures of the strong-current regions of B and C.

(A color version of this figure is available in the online journal.)

Nevertheless, we note that the misalignments between the modeling field lines and the observations are also obvious, especially for the large loops near the northwest boundary of the FoV. There are several reasons for the misalignments: first, a local Cartesian coordinate system is not adequate to include the large loops which obviously require spherical geometry; second, the FoV of magnetogram may not be large enough to properly characterize the entire relevant current system, which again requires the curvature of the Sun's surface to be taken into account; third, it is not easy to precisely locate the photospheric footpoints of different loops that spread apart distinctly in the corona but are rooted very closely in the photosphere; fourth, the coronal field may be rather dynamic, e.g., it expands or oscillates due to eruptions, which makes the static extrapolation fail. We know that this visual comparison between the model result and observation is very preliminary, and further critical comparison is required, for example, with the 3D loops reconstructed with multi-points observation (DeRosa et al. 2009; Aschwanden 2011).

Routinely, we check the quality of the numerical result by computing several metrics. The force-freeness of the extrapolation data is usually measured by a current-weighted sine metric (CWsin) defined by

$$\mathrm{CWsin} \equiv \frac{\int_V J\sigma dV}{\int_V J dV}; \quad \sigma = \frac{\mathbf{J}\times\mathbf{B}}{JB}, \tag{8}$$

where $B = |\mathbf{B}|$, $J = |\mathbf{J}|$ and $V$ is the computational volume. We also compute a current-square-weighted sine metric ($C^2$Wsin) similarly defined by

$$C^2\mathrm{Wsin} \equiv \frac{\int_V J^2\sigma dV}{\int_V J^2 dV}, \tag{9}$$

with more weight on the strong-current regions. The divergence-freeness is measured by $\langle|f_i|\rangle$

$$\langle|f_i|\rangle = \frac{1}{V}\int_V \frac{\nabla\cdot\mathbf{B}}{6B/\Delta x} dV. \tag{10}$$

We care about different energy contents, i.e., the total energy $E_{\rm tot}$, the potential energy $E_{\rm pot}$ and the free energy $E_{\rm free}$

$$E_{\rm tot} = \int_V \frac{B^2}{8\pi} dV, \quad E_{\rm pot} = \int_V \frac{B_{\rm pot}^2}{8\pi} dV, \quad E_{\rm free} = E_{\rm tot} - E_{\rm pot}, \tag{11}$$

where $B_{\rm pot}$ is the potential field strength. The results of the metrics are given in Table 2 for extrapolations from both the raw and preprocessed magnetograms. We compute the metrics for four different regions including the full extrapolation box and the subregions A, B, and C as outlined in Figure 6.

For the full region, our results of the current-weighted sine is ~0.3, which means that the mean misalignment angle between the magnetic field and current is about 17°. This value is much larger than those from our previous benchmark tests using ideal or synthetic magnetograms (which are ~0.1 (6°) or smaller; see Jiang & Feng 2012), but is comparable to previously reported results by other NLFFF codes on real magnetograms (e.g., the average CWsin by various NLFFF codes applied to AR 10930 (Schrijver et al. 2008) and AR 10953 (DeRosa et al. 2009) are 0.36 and 0.28, respectively). With such a large misalignment angle, the result seems to be far away from an exactly force-free solution which has a zero misalignment angle. However, it should be noted that the metric CWsin may not be a good monitor for numerical solutions, which unavoidably have random numerical errors because of

**Table 2**
Results of the Metrics for AR 11158

| Region | CWsin | $C^2$Wsin | $\langle \lvert f_i \rvert \rangle$ | $E_{\rm tot}$ | $E_{\rm pot}$ | $E_{\rm free}$ | $E_{\rm free}/E_{\rm pot}$ | $E_{\rm free}/(E_{\rm free})_{\rm full}$ |
|---|---|---|---|---|---|---|---|---|
| Raw | | | | | | | | |
| Full | 0.32 | 0.18 | 6.59E-04 | 10.9 | 8.97 | 1.93 | 22% | 100% |
| A | 0.18 | 0.11 | 1.25E-03 | 8.3 | 6.24 | 2.06 | 33% | 107% |
| B | 0.07 | 0.06 | 7.17E-04 | 3.24 | 2.09 | 1.15 | 55% | 60% |
| C | 0.16 | 0.11 | 1.64E-03 | 0.67 | 0.47 | 0.20 | 43% | 10% |
| Preprocessed | | | | | | | | |
| Full | 0.30 | 0.14 | 6.18E-04 | 9.83 | 8.18 | 1.65 | 20% | 100% |
| A | 0.17 | 0.10 | 1.20E-03 | 7.54 | 5.61 | 1.93 | 34% | 117% |
| B | 0.06 | 0.05 | 7.20E-04 | 2.97 | 1.81 | 1.16 | 64% | 70% |
| C | 0.16 | 0.12 | 1.67E-03 | 0.59 | 0.42 | 0.17 | 40% | 10% |

**Notes.** Full region is extrapolation box of $[0, 300](x) \times [0, 300](y) \times [0, 150](z)$. Region A is $[53, 222] \times [104, 191] \times [0, 50]$; Region B is $[116, 181] \times [145, 175] \times [0, 30]$; Region C is $[62, 102] \times [132, 161] \times [0, 20]$. The FoVs of the regions are shown by the boxes in Figure 6. The energy unit is $10^{32}$ erg.

limited resolution. As a simple example, CWsin is close to 1 even for a potential field solution computed by Green's function method or other numerical realization. This is because the numerical difference, used for computing the current $\mathbf{J} = \nabla \times \mathbf{B}$ from $\mathbf{B}$, gives small but finite currents whose directions are randomly from 0° to 180°; thus an average of the full volume should give a misalignment angle of ∼90°. The noise in the observation data, mainly in the weak field regions, is also a major source for random numerical errors. In these regions, the actual magnetic elements are probably smaller than the observed or numerical pixel size, and the field directions generally exhibit a random pattern on the image. To reduce such errors in computing the metric, we can either increase the weight of the current (e.g., use $C^2$Wsin) or compute CWsin within the strong-current subregions only. As is expected, the misalignment angle decreases significantly by measuring in this way. For the full region, $C^2$Wsin are only half that of CWsin. For the subregions, CWsin is also only half or less for the full region, reaching the level of those from the benchmark tests (Jiang & Feng 2012). In particular, the misalignment angle is only about 4° in subregion B, showing that the force-free assumption is modeled very well.

Regarding the energy contents, it is interesting to note that the free energy of subregion A exceeds that of the full region, meaning that the free energy content in the full volume excluding subregion A is negative. This is, however, not surprising as we know that any sub-volume energy content of the non-potential field may be lower than the potential energy (e.g., Mackay et al. 2011; Jiang et al. 2012a). Also the measurement error may result in this negative free energy since it is very small compared to the total free energy. Regardless of which case is true, it can be clearly seen that the spatial distribution of free energy is largely co-spatial with that of the current, since the subregion A contains most of the currents of the entire volume. This confirms that the free energy in the corona is actually stored by the current-carrying field (where non-potentiality is strong), but not necessarily in the magnetic flux concentrations.

Finally, we compare the results extrapolated from the raw and preprocessed magnetograms. Inspecting the force-freeness and divergence-freeness metrics shows that the improvement by preprocessing is negligible. This is because the raw data already satisfies the boundary force-free conditions well. Due to the smoothing, the result for the preprocessed data gives slightly lower energy content than those for the raw data.

### *4.2. AR 11283*

Figure 7 compares the AIA 171 Å loops with the reconstructed field in the same way as Figure 5. For this AR, the NLFFF model appears to perform only slightly better than the potential model (there are some loops even produced by the NLFFF model that are even worse than the potential model near the northeast boundary of the FoV). The clearest misalignment with the observation is the large closed loop pointed by the arrow in the AIA image. The potential and force-free models failed to recover this group of loops and give open field lines instead. This, however, is not unexpected since the inputted magnetogram has flux unbalanced by −10%. So there must be field lines from the negative polarity opening in the FoV. The reason for this flux unbalance may be that the positive flux in the east is rather dispersed (much more than the negative polarity), and thus properly be underestimated by the observation.

Near the major polarity the structure of the loops is very complex and the extrapolated field shows highly sheared and twisted structures, indicating a significant non-potentiality there. Actually this was the site of the flare and filament eruption. The distribution of the vertically integrated current shows a strong concentration of current in this region, as denoted by A in Figure 8. In the same figure, we show the local field structure and the observations from different wavelengths of much higher temperature than 171 Å. The magnetic field exhibits a multi-flux rope configuration. The most remarkable structure is a sigmoid, i.e., the S-shaped loop in the AIA 94 Å and 335 Å images. The sigmoid can be seen most clearly in the AIA 94 Å wavelength (6.3 MK) with rather thin but enhanced shape, and is also well shaped in the soft X-ray image taken by *Hinode*/XRT. In the fourth panel of the figure the field lines are plotted overlying on the AIA 94 Å image. It demonstrates that our extrapolation has recovered the sigmoid rather precisely, at least in morphology (see the precise alignment of the field lines with the shape of the sigmoid). The distribution of the current also roughly resembles the shape of the sigmoid, suggesting that the enhancement of EUV and X-ray emission associated with the sigmoid is made by the strong field-aligned current via Joule heating of the plasma. This sigmoid is located between the major positive and negative polarities and the currents reside mostly in the northeast part, as shown by the current distribution. The twist of the sigmoid field lines is not strong as modeled in other cases such as Roussev et al. (2012) or Savcheva et al. (2012), and this sigmoid is

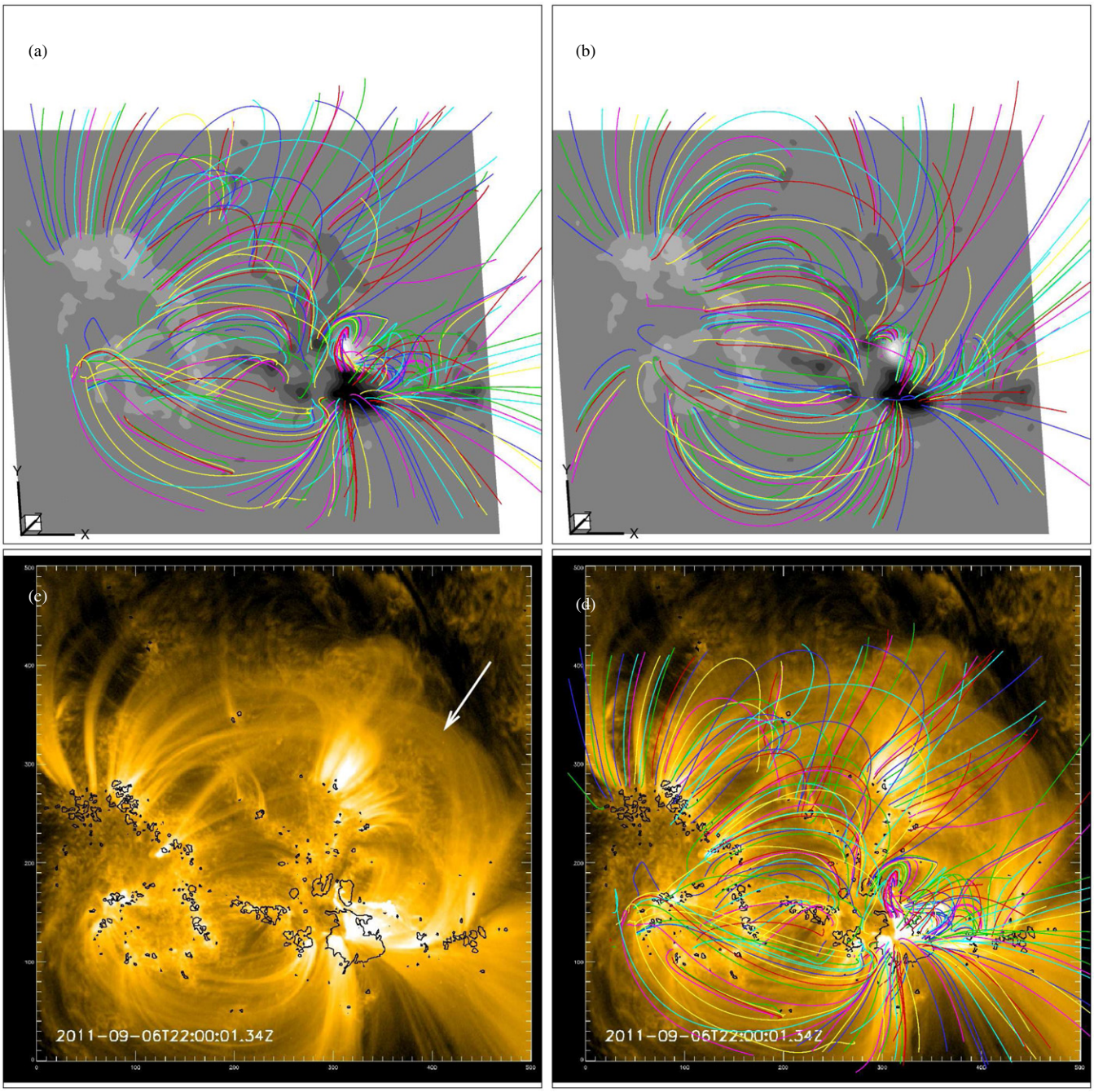


**Figure 7.** Same as Figure 5 but for AR 11283.
(A color version of this figure is available in the online journal.)

composed of a single flux rope, which is also different from their results with two flux ropes or double-J shaped current pattern. The observation and modeling suggest that there seems to be another flux rope overlying the sigmoid, and the flare and CME may result from the eruptions of these flux ropes, which is left for future study.

Similarly, we compute the metrics of force-freeness and divergence-freeness for both the full region and the subregion and the results are given in Table 3. By comparing the results using the raw and preprocessed data, we find that evidently the preprocessed result is closer to force free, especially of the full region for which the raw data gives CWsin $\sim 0.4$ (24°) while the preprocessed data gives CWsin $\sim 0.3$ (17°). Thus for this AR the preprocessing indeed improves the extrapolation greatly. Also the divergence is reduced by the preprocessing. It is noticeable that the total energy content is doubled by the preprocessing, reaching $10^{32}$ erg. However, even this improvement of the free energy is likely to underestimate the actual value, considering that a X-class flare and CME erupted immediately (Feng et al. 2013). Still, the current is strongly localized and the free energy is concentrated within the strong-current region, i.e., subregion A, which occupies only less than one percent of the full volume, but contains most of the free energy.

### *4.3. Convergence Study*

It is important to monitor the relaxation process in order to study whether the iteration converges, since there is no theory to guarantee this. Here we study the convergence process of

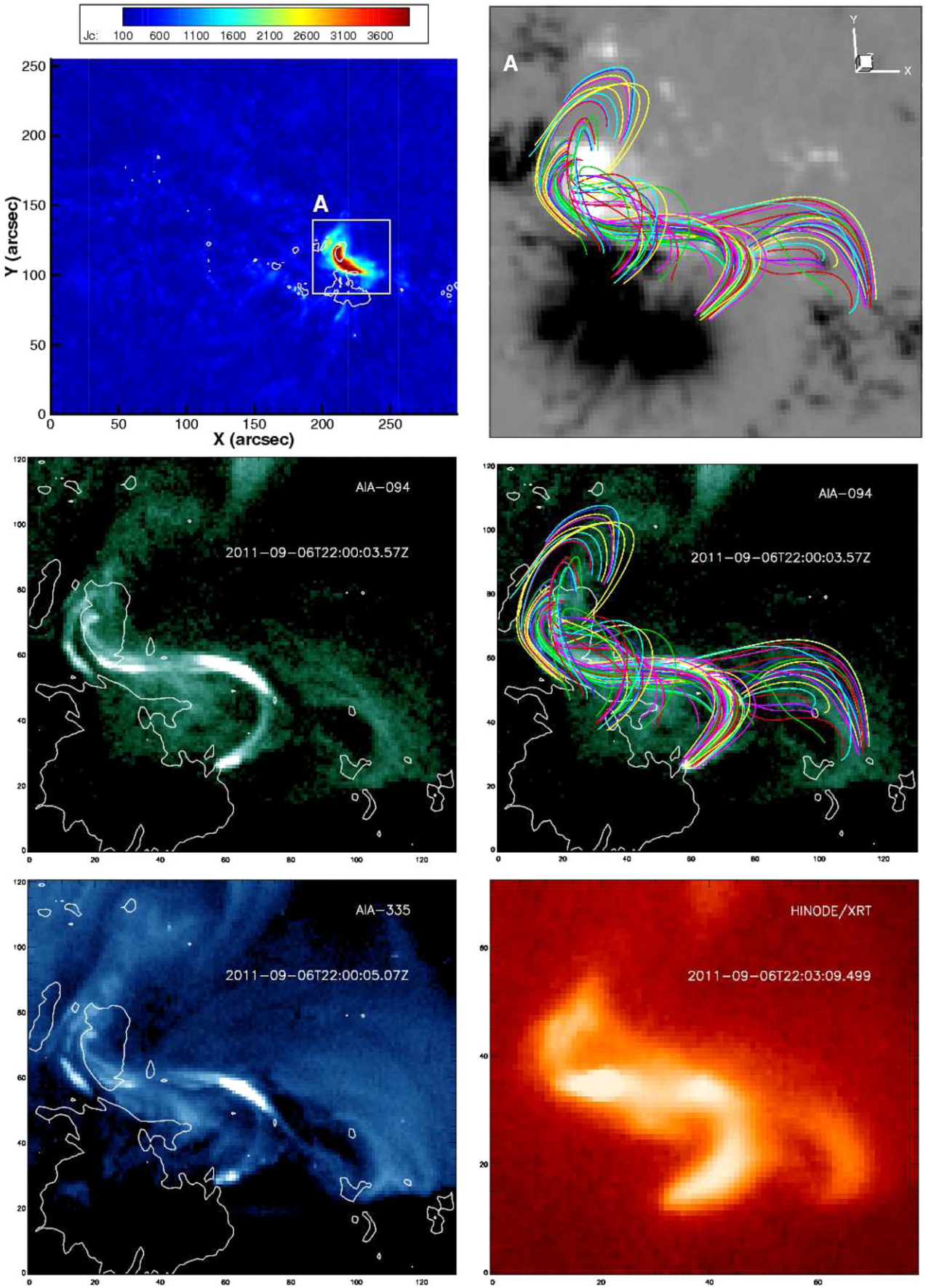


**Figure 8.** Strong-current region and its magnetic structure for AR 11283. The upper left panel is an image of the vertical integral of the current density, i.e., $J_C = \int |\mathbf{J}| dz$; and the upper right panel shows the magnetic structure of subregion A, where a sigmoid, shown in the following panels, is observed clearly by *SDO*/AIA and *Hinode*/XRT.

(A color version of this figure is available in the online journal.)

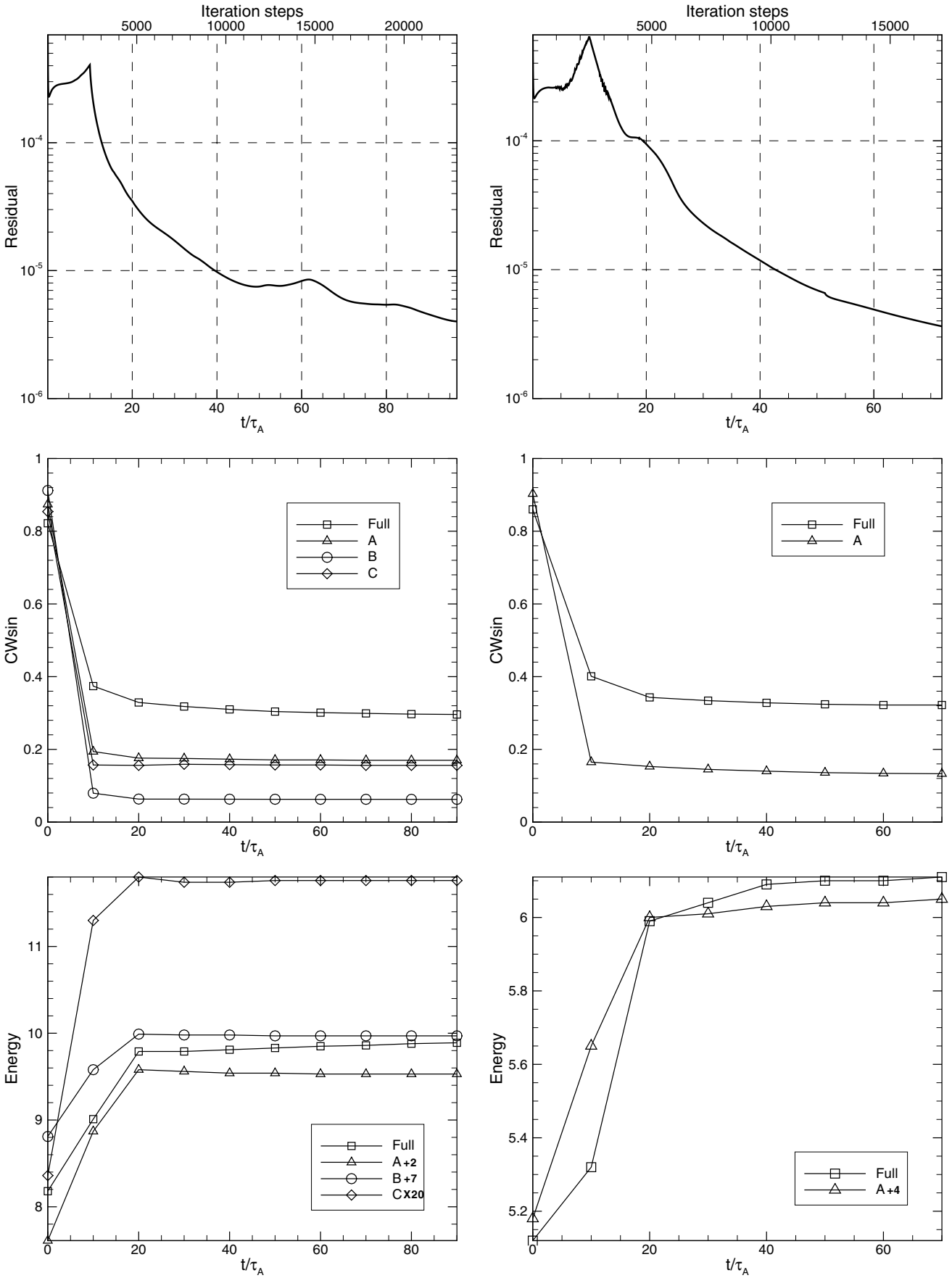


**Figure 9.** Convergence of computations: temporal evolution of the residual, the metric CWsin, and the total energy content in the iteration process for AR 11158 (left column) and AR 11283 (right column). Note that for a better plot for the energy contents of different regions, their values are scaled properly as shown in the legends.

**Table 3**
Results of the Metrics for AR 11283

| Region | CWsin | C$^2$Wsin | $\langle \lvert f_i \rvert \rangle$ | $E_{\rm tot}$ | $E_{\rm pot}$ | $E_{\rm free}$ | $E_{\rm free}/E_{\rm pot}$ | $E_{\rm free}/(E_{\rm free})_{\rm full}$ |
|---|---|---|---|---|---|---|---|---|
| Raw | | | | | | | | |
| Full | 0.40 | 0.24 | 9.65E-04 | 5.94 | 5.58 | 0.46 | 8% | 100% |
| A | 0.15 | 0.09 | 3.69E-03 | 1.86 | 1.33 | 0.53 | 40% | 115% |
| Preprocessed | | | | | | | | |
| Full | 0.32 | 0.18 | 8.28E-04 | 6.10 | 5.12 | 0.98 | 19% | 100% |
| A | 0.13 | 0.09 | 1.76E-03 | 2.05 | 1.18 | 0.87 | 74% | 89% |

**Notes.** Full region is extrapolation box of $[0, 300](x) \times [0, 256](y) \times [0, 150](z)$. Region A is $[193, 251] \times [86, 140] \times [0, 30]$. The FoVs of the regions are shown by the box in Figure 8. The energy unit is $10^{32}$ erg.

the computations by temporal evolution of several monitors, including the residual of the field between two successive iterations

$$\mathrm{res}^n(\mathbf{B}) = \sqrt{\frac{1}{3}\sum_{\delta=x,y,z}\frac{\sum_i \left(B^n_{i\delta} - B^{n-1}_{i\delta}\right)^2}{\sum_i \left(B^n_{i\delta}\right)^2}} \qquad (12)$$

(where $n$ denotes the iteration step), the metric CWsin, and the total energy content. We record the residual by every ten steps and compute CWsin and total energy by every ten $\tau_{\rm A}$. The results for extrapolation of both ARs are plotted in Figure 9. As can be seen, the system converges smoothly and fast. During the first 10 $\tau_{\rm A}$, the residual continues to increase because the transverse field is inputted at the bottom continuously, which drives the system away from the initial potential field. After this driving process, the residual drops immediately, indicating a fast relaxation of the system. With about 40 $\tau_{\rm A}$ (nearly 10000 iterations), the residual is already reduced to $\sim 10^{-5}$, and all the metrics and energy almost stagnate afterward. Thus the computations can actually be terminated once the residual is below $10^{-5}$, which is consistent with our previous studies for benchmark cases (Jiang & Feng 2012; Jiang et al. 2012b). It is also noteworthy that the convergence process is rather smooth, without any obvious oscillation or abrupt variation of the residual or the metrics, so the iteration is "safe." This is a good feature of our code over other iteration codes for extrapolation, e.g., the Valori et al.'s (2007) magnetofrictional code or the Wheatland's (2006) Grad-Rubin-like code, which usually show strong oscillatory in the iteration or even fail to converge occasionally (Schrijver et al. 2008; DeRosa et al. 2009).

## 5. CONCLUSIONS

In this paper we have applied the CESE–MHD–NLFFF code to the *SDO*/HMI vector magnetograms. Two ARs are sampled for the test, AR 11158 and AR 11283, both of which produced X-class flares and were very non-potential. We compared the results with the *SDO*/AIA images, showing that the reconstructed field lines resemble well most of the plasma loops, which is a basic requirement for an applicable NLFFF modeling code (DeRosa et al. 2009). Because the magnetic flux of the AR 11283 magnetogram is not well balanced, the extrapolation of the large scale field does not appear to be as good as that for AR 11158. Observations show that there were filaments or sigmoids in the core regions of the ARs which are important precursors of eruptions such as flares and CMEs. We also found that in these places there were highly sheared and twisted field lines, i.e., flux ropes, which contain strong field-aligned currents and plenty of non-potential energy, and our extrapolations recovered well those observed features, especially the sigmoid in AR 11283. By computing the metric CWsin, which measures the mean value of misalignment between the magnetic field and electric current, we found that, the force-free constraint is fulfilled very well in the strong-field regions (CWsin $\approx$0.1, misalignment about 6°) but apparently not that well in the weak-field regions (CWsin $\approx$0.3, misalignment about 17°) because of the noise in the data and numerical errors of the small currents. The energy contents of our results are also consistent with the previous computations (with respect to the AR 11158, e.g., Wiegelmann et al. 2012; Sun et al. 2012b). In summary, our extrapolation code can be used as a viable tool to study the 3D magnetic field in the corona.

We developed the CESE–MHD–NLFFF code not only for field extrapolation, but also as a sub-program for the project of data-driven MHD modeling of the ARs, the eruptions and their dynamic evolutions in the global corona using continuously observed data on the photosphere. At present numerical MHD investigations of the solar eruptions (Amari et al. 2003; MacNeice et al. 2004; Aulanier et al. 2009; Fan 2010; Török et al. 2011; Roussev et al. 2012) are mostly based on idealized magnetic configurations without constrained by real observations. A step forward in understanding what really happens in the solar eruptions certainly necessitates the observation-constrained numerical model. For example, considering that NLFFF extrapolation can recover highly sheared magnetic arches and twisted flux ropes, which are basic building blocks of many eruption models (e.g., Török & Kliem 2005; Aulanier et al. 2009), utilizing the extrapolated field from real magnetograms can obviously provide much more realistic initial inputs than those idealized models like Titov & Démoulin's (1999) flux rope model. Our future work will input the extrapolation field as an initial condition into the data-driven full MHD model (Jiang et al. 2012a; Feng et al. 2012), along with the surface plasma flows derived from time-series of photosphere magnetograms (e.g., Liu et al. 2012) as a bottom boundary condition to stress the model, with an objective to better simulate the initiation and evolution of solar explosive phenomena and their interplanetary evolution process.

This work is jointly supported by the 973 program under grant 2012CB825601, the Chinese Academy of Sciences (KZZD-EW-01-4), the National Natural Science Foundation of China (41204126, 41274192, 41031066, and 41074122), and the Specialized Research Fund for State Key Laboratories. Data are courtesy of NASA/SDO and the HMI science teams. C. W. Jiang thanks Dr. X. Luo for a careful revision of the text. The authors thank the anonymous referee for invaluable comments.

## REFERENCES


Aly, J. J. 1989, SoPh, 120, 19
Amari, T., Aly, J. J., Luciani, J. F., Boulmezaoud, T. Z., & Mikic, Z. 1997, SoPh, 174, 129
Amari, T., Boulmezaoud, T. Z., & Mikic, Z. 1999, A&A, 350, 1051
Amari, T., Luciani, J. F., Aly, J. J., Mikic, Z., & Linker, J. 2003, ApJ, 585, 1073
Aschwanden, M. J. 2011, LRSP, 8, 5
Aschwanden, M. J., Wuelser, J.-P., Nitta, N. V., et al. 2012, ApJ, 756, 124
Aulanier, G., Török, T., Démoulin, P., & DeLuca, E. E. 2009, ApJ, 708, 314
Borrero, J., Tomczyk, S., Kubo, M., et al. 2011, SoPh, 273, 267
DeRosa, M. L., Schrijver, C. J., Barnes, G., et al. 2009, ApJ, 696, 1780
Fan, Y. 2010, ApJ, 719, 728
Feng, L., Wiegelmann, T., Su, Y., et al. 2013, ApJ, 765, 37
Feng, X., Jiang, C., Xiang, C., Zhao, X., & Wu, S. 2012, ApJ, 758, 62
Feng, X., Yang, L., Xiang, C., et al. 2012, SoPh, 279, 207
Inoue, S., Kusano, K., Magara, T., Shiota, D., & Yamamoto, T. T. 2011, ApJ, 738, 161
Jiang, C. W., Feng, X., Fan, Y., & Xiang, C. 2011, ApJ, 727, 101
Jiang, C. W., Feng, X., Wu, S. T., & Hu, Q. 2012a, ApJ, 759, 85
Jiang, C. W., Feng, X., & Xiang, C. 2012b, ApJ, 755, 62
Jiang, C. W., & Feng, X. S. 2012, ApJ, 749, 135
Jiang, C. W., Feng, X. S., Zhang, J., & Zhong, D. K. 2010, SoPh, 267, 463
Jing, J., Park, S.-H., Liu, C., et al. 2012, ApJL, 752, L9
Leka, K., Barnes, G., Crouch, A., et al. 2009, SoPh, 260, 83
Liu, Y., Zhao, J., & Schuck, P. W. 2012, SoPh, 195
Low, B. C., & Lou, Y. Q. 1990, ApJ, 352, 343
Mackay, D. H., Green, L. M., & van Ballegooijen, A. 2011, ApJ, 729, 97
MacNeice, P., Antiochos, S. K., Phillips, A., et al. 2004, ApJ, 614, 1028
Malanushenko, A., Schrijver, C. J., DeRosa, M. L., Wheatland, M. S., & Gilchrist, S. A. 2012, ApJ, 756, 153
McClymont, A. N., Jiao, L., & Mikic, Z. 1997, SoPh, 174, 191
Metcalf, T. R., DeRosa, M. L., Schrijver, C. J., et al. 2008, SoPh, 247, 269
Metcalf, T. R., Jiao, L., McClymont, A. N., Canfield, R. C., & Uitenbroek, H. 1995, ApJ, 439, 474
Molodenskii, M. M. 1969, SvA, 12, 585
Roumeliotis, G. 1996, ApJ, 473, 1095
Roussev, I., Galsgaard, K., Downs, C., et al. 2012, NatPh, 8, 845
Sakurai, T. 1989, SSRv, 51, 11
Savcheva, A. S., van Ballegooijen, A. A., & DeLuca, E. E. 2012, ApJ, 744, 78
Schrijver, C. J., Aulanier, G., Title, A. M., Pariat, E., & Delannée, C. 2011, ApJ, 738, 167
Schrijver, C. J., DeRosa, M. L., Metcalf, T. R., et al. 2006, SoPh, 235, 161
Schrijver, C. J., DeRosa, M. L., Metcalf, T., et al. 2008, ApJ, 675, 1637
Sun, X., Hoeksema, J. T., Liu, Y., Chen, Q., & Hayashi, K. 2012a, ApJ, 757, 149
Sun, X., Hoeksema, J. T., Liu, Y., et al. 2012b, ApJ, 748, 77
Titov, V. S., & Démoulin, P. 1999, A&A, 351, 707
Török, T., & Kliem, B. 2005, ApJL, 630, L97
Török, T., Panasenco, O., Titov, V. S., et al. 2011, ApJL, 739, L63
Turmon, M., Jones, H. P., Malanushenko, O. V., & Pap, J. M. 2010, SoPh, 262, 277
Valori, G., Kliem, B., & Fuhrmann, M. 2007, SoPh, 245, 263
Wheatland, M. S. 2006, SoPh, 238, 29
Wheatland, M. S., Sturrock, P. A., & Roumeliotis, G. 2000, ApJ, 540, 1150
Wiegelmann, T. 2004, SoPh, 219, 87
Wiegelmann, T. 2008, JGR, 113, 3
Wiegelmann, T., Inhester, B., & Sakurai, T. 2006, SoPh, 233, 215
Wiegelmann, T., & Sakurai, T. 2012, LRSP, 9, 5
Wiegelmann, T., Thalmann, J. K., Inhester, B., et al. 2012, SoPh, 281, 37
Wu, S. T., Sun, M. T., Chang, H. M., Hagyard, M. J., & Gary, G. A. 1990, ApJ, 362, 698
Yan, Y., & Sakurai, T. 2000, SoPh, 195, 89
Yang, L. P., Feng, X. S., Xiang, C. Q., et al. 2012, JGRA, 117, 8110